Electrical and magnetic properties of $La_{0.67}Ba_{0.33}Mn_{1-x}(Me)_xO_3$ perovskite manganites : case of manganese substituted by trivalent (Me=Cr) and tetravalent (Me=Ti) elements

Marwène Oumezzine [a,b*], Octavio Peña [b], Sami Kallel [a], Nabil Kallel [a], Thierry Guizouarn [b], Francis Gouttefangeas[c], Mohamed Oumezzine [a]

[a] *Laboratoire de Physico-chimie des Matériaux, Département de Physique, Faculté des Sciences de Monastir, Université de Monastir, 5019, Tunisia.*

[b] *Institut des Sciences Chimiques de Rennes, UMR 6226, Université de Rennes 1, 35042 Rennes cedex, France.*

[c] *C.M.E.B.A (Centre de Microscopie Electronique à Balayage et microanalyse) , Université de Rennes 1, 35042 Rennes cedex, France.*

**. Corresponding author.* (Ma.Oumezzine)

E-mail: Oumezzine@hotmail.co.uk

marouan.omezzine@etudiant.univ-rennes1.fr

Phone: +216 22 773 676, +33(0) 635 523 961, Fax: +216 73 500 278

Abstract:

The effect of non-magnetic Ti^{4+} substitution on the structural, electrical and magnetic properties of $La_{0.67}Ba_{0.33}Mn_{1-x}Ti_xO_3$ ($0 \leq x \leq 0.1$) are investigated and compared to those existing in $La_{0.67}Ba_{0.33}Mn_{1-x}Cr_xO_3$, (magnetic Cr^{3+}). The structural refinement by the Rietveld method revealed that Ti-doped samples crystallize in the cubic lattice with space group $P\,m\bar{3}m$, while samples with Cr crystallize in the hexagonal setting of the rombohedral $R\bar{3}C$ space group for identical contents of dopant. The most relevant structural features are an increase of the lattice parameters, of the cell volume and of the inter-ionic distances with increasing Ti doping level. Both series of samples show a decrease of the paramagnetic-ferromagnetic transition temperature (T_C) when the amount of chromium or titanium increases. Transport measurements show that when increasing the metal doping, the resistivity increases whereas the metallic behaviour of the parent compound $La_{0.67}Ba_{0.33}MnO_3$ is destroyed. For a substitution higher than 5 at.% of Ti and 10 at.% of Cr, the samples exhibit a semiconducting behaviour in the whole range of temperature, for which the electronic transport can be explained by a variable range hopping (VRH) and/or small polaron hopping (SPH) models.

Keywords: Manganites, Mn-doping, Resistivity, Transport mechanism, Magnetic properties

1- Introduction

Manganese oxides $R_{1-x}A_xMnO_3$ (R, a trivalent rare-earth element, e.g. La, Nd, Pr, and A, a divalent dopant, e.g Ca, Ba and Sr) of perovskite structure have been extensively investigated since the discovery of the phenomenon of colossal magnetoresistance (CMR) [1-4]. The microscopic mechanism underlying the electronic, structural and magnetic properties in these materials can be characterized by a delicate interplay of spin, charge and lattice degrees of freedom [5-7]. Presence of holes (Mn^{4+}) into the Mn^{3+} e_g orbitals creates ferromagnetic double-exchange interactions (DE) which couple magnetism with electrical conductivity [8], while the Jahn-Teller distorted-ions Mn^{3+} couple magnetism with the lattice. Both the electronic and magnetic properties of the perovskite compounds are sensitive to the effective d-electron hopping interaction and nominal concentrations. In addition, doping not only changes the structural tolerance factor (t_G) but also changes the Mn-O-Mn bond angles, which strongly affects the electron hopping process between Mn^{3+} and Mn^{4+} ions and the associated conduction mechanism. By this way, one can tailor the properties of these manganites in a more effective way. So, it is expected then, that substitution of Mn by trivalent and tetravalent elements will strongly affect the electronic, transport and magnetic behaviour of these compounds [9-13].

In the present work, we examine the influence of Ti-substitution on the structural, magnetic and electrical transport properties of $La_{0.67}Ba_{0.33}Mn_{1-x}Ti_xO_3$ ($0 \leq x \leq 0.1$). Titanium is a quite stable tetravalent element in transition-metal oxides [14]; it is a nonmagnetic cation and therefore no interactions between Ti^{4+} and Mn^{3+} ions will occur. Because of its tetravalent oxidation state the total number of 3d electrons should decrease linearly with increasing Ti-doping. With this in mind, it becomes interesting to compare the physical properties of the

Ti-doped manganite perovskites with those of Cr-doped (trivalent Cr^{3+}) system. In a parallel work presented elsewhere, we have reported the physical properties of the solid solution $La_{0.67}Ba_{0.33}Mn_{1-x}Cr_xO_3$ ($0 \leq x \leq 0.15$) perovskites [15]. The results showed that substitution of Mn by trivalent Cr^{3+} leads to drastic changes in their physical properties.

From the relationship between the average (Mn/Ti–O) and (Mn/Cr–O) distances and their influence on the magnetic and electrical properties, we will make clear the role of the tetravalent and trivalent ions in the ferromagnetic-to-paramagnetic and metal-to-semiconductor transitions. Thus, Ti and Cr doping at the Mn-site should provide useful information for the understanding of the main physical mechanisms existing in these manganite perosvkites.

2- Experimental details

Polycrystalline samples of nominal compositions $La_{0.67}Ba_{0.33}Mn_{1-x}Ti_xO_3$ ($0 \leq x \leq 0.1$) were synthesized by a conventional solid-state reaction method. Raw materials of La_2O_3, $BaCO_3$, Mn_2O_3 and TiO_2, of purities higher than 99%, were weighed in stoichiometric amounts. The mixtures were heated in air at 900°C for 72h to achieve decarbonisation. The material was then ground in an agate mortar to have fine powder. The calcined mixtures were then pressed into pellets (13mm diameter and 2mm thickness under 8Tons/cm^2) and sintered several times in air, with intermediate grindings, at 1400° C for 48h.

The morphological properties of the samples were investigated by scanning electron microscopy (SEM) on a JSM-6400 apparatus working at 20 KV. The structural characterization was done through X-ray diffraction patterns (XRD) using a “Panalytical X pert Pro” diffractometer with Cu Kα radiation (λ=1.5406 $\mathring{A}$). Data for Rietveld refinement were collected in the range of 2θ from 10 to 120° with a step size of 0, 017° and a counting time of 18s per step. The magnetization was measured in a ZFC/FC mode between 2K and 400 K, under a magnetic field of 100 Oe, using a Quantum Design SQUID susceptometer,

model MPMS-XL5. The temperature dependence of the d.c resistivity ρ(T) was measured by the conventional four-probe method in the range 80-300K.

3- Structural and morphological properties

The X-ray diffraction patterns for the series $La_{0.67}Ba_{0.33}Mn_{1-x}Ti_xO_3$ ($0 \le x \le 0.1$) show that all samples are single phase, with no detectable impurities (Figure 1). All diffraction peaks have been indexed in a cubic lattice symmetry with space group $Pm\bar{3}m$, while patterns for the series $La_{0.67}Ba_{0.33}Mn_{1-x}Cr_xO_3$ were indexed on the basis of a rombohedral-distorted perovskite structure in the $R\bar{3}C$ space group for samples with $x \le 0.1$ and in a cubic lattice with $Pm\bar{3}m$ space group for x=0.15 [15]. These observations are consistent with the values of the Goldschmidt tolerance factor t_G (Table I), $t_G=(r_O+r_A)/\sqrt{2}\,(r_O+r_B)$ [16], where r_A, r_B and r_O are respectively the average ionic radii of the A and B perovskite sites and of the oxygen anion. The tolerance factor is an important structural parameter which reflects the local microscopic distortion from the ideal perovskite (ABO_3) structure ($t_G=1$), for which the B-O-B bond angle θ is equal to 180°.

The structural parameters were refined by the standard Rietveld technique using the FullProf program [17], based on the consideration of low values of the residuals for the weighted pattern R_{WP}, the pattern R_P, the structure factor R_F and the goodness of fit χ^2, as listed in Table I. An excellent agreement was found between the experimental spectra and the calculated values (Fig.2). The lattice parameters and the unit cell volume of $La_{0,67}Ba_{0,33}Mn_{1-x}Ti_xO_3$ ($0 \le x \le 0.1$) increase monotonously with increasing the Ti-doping , as shown in Figure 3 and Table I. The increase of the lattice constant can be related to the larger ionic radius of the Ti ion (r_{Ti4+}=0.605 $\mathring{A}$, and r_{Mn4+}=0.54 $\mathring{A}$). This is confirmed by the evaluation of the (Mn,Ti)-O bond length distance using Rietveld refinement, which also increases with Ti doping (Table I). Thus, the linear increase in $d_{(Mn,\ Ti)-O}$ with the nominal Ti

content x is in agreement with our starting hypothesis of a Mn^{4+}-Ti^{4+} substitution. The obtained angles (180°) confirm the cubic structure of all samples.

Our results are similar to those reported for the $La_{0.7}Sr_{0.3}Mn_{1-x}Ti_xO_3$ system [18] for which an increase in the Ti content does not appreciably change the (Mn,Ti)-O-(Mn,Ti) bond angle although it results in an increase of the (Mn,Ti)-O bond length and of the corresponding lattice parameters.

Compared with the substitution of Mn^{3+} by Cr^{3+} in $La_{0.67}Ba_{0.33}Mn_{1-x}Cr_xO_3$, we observe that the lattice parameters a and c, the unit cell volume and the (Mn, Cr)-O-(Mn, Cr) bond angle decrease with increasing Cr content (Table II), which was attributed to the smaller ionic radius of the Cr^{3+} ions ($0.62\,\mathring{A}$) substituting the larger Mn^{3+} ions ($0.64\,\mathring{A}$) [15].

Figure 4 depicts the scanning electron micrograph (SEM) images taken for $La_{0.67}Ba_{0.33}Mn_{1-x}Ti_xO_3$ samples with x=5 at.%, x=7 at.% and x=10 at.%. All samples are composed of strongly connected large grains, forming almost homogenous particles.

The crystallites size was estimated using the XRD data and applying the Rietveld refinement formula:

$$G_S = \frac{180\lambda}{\pi\sqrt{IG}} \qquad \textbf{(1)}$$

where λ is the X-ray wavelength and IG is the Gaussian size parameter given by the Rietveld refinement. The average grain size (G_S) estimated by this analysis is approximately 30 nm.

4-Physical properties

4-1-Magnetic properties

The effect of the substitution of nonmagnetic Ti^{4+} for a magnetic ion Mn^{4+} on the physical properties of $La_{0.67}Ba_{0.33}Mn_{1-x}Ti_xO_3$ ($0 \le x \le 0.1$) was studied through the temperature dependence of the magnetization M(T). Figure 5 (a) shows the zero-field cooled/field-cooled (ZFC/FC) cycles measured under a magnetic field of 100 Oe.

All samples present a magnetic transition from a paramagnetic state at high temperatures, to a ferromagnetic state at low temperatures. The Curie ordering temperature T_C, was evaluated from the minimum value of the temperature derivative of the magnetization in FC mode, dM/dT (inset, figure 5 (a)). The transition temperature decreases systematically with increasing Ti concentrations, from 345K for x=0 to 183K for x=0.1 (Figure 5b). A similar behaviour was observed for the Cr-substituted manganites $La_{0.67}Ba_{0.33}Mn_{1-x}Cr_xO_3$ although less pronounced (figure 5b and Table III) [15].

As it is well known, the magnetic and transport properties of double-exchange ferromagnets are controlled by the one-electron bandwidth *W*, which is determined by the average radius of the A-cations $<r_A>$ through the $\theta_{Mn\text{-}O\text{-}Mn}$ bond angles [19]:

$$W \alpha \frac{\cos[(\Pi - \gamma)/2]}{< d_{Mn-O} >^{3.5}} \qquad \textbf{(2)}$$

where γ is the average bond angle $<\theta_{Mn\text{-}O\text{-}Mn}>$, and $<d_{Mn\text{-}O}>$ is the average bond length. We suggest that the reduction of T_C should be attributed to the reduction of the one-electron bandwidth *W* (Table I). The ferromagnetic transition temperature and the magnetization decrease with increasing amount of titanium. On the other hand, the T_C values of the Cr-doped samples are higher than those of the Ti-doped samples, that is, the decrease with x is more sensitive to the Ti-substitution compared to the Cr-one (figure 5 (b)). The slow decrease of T_C in Cr-doped compounds as x increases is in agreement with the weakness of the Mn^{3+}-O-Mn^{4+} and Mn^{3+}-O-Cr^{3+} ferromagnetic interactions, indicating that the Mn^{3+} cations are mainly replaced by the Cr^{3+} ions [15]. Ti^{4+} ion is non magnetic and does not possess any 3d electrons, but its presence in the crystal lattice substituting Mn causes a sudden break of the ferromagnetic Mn^{3+}-O-Mn^{4+} interactions without any ferromagnetic compensation, leading to a much stronger decrease of T_C than in the case of Cr substitution.

4-2- Electrical transport properties

The temperature dependence of the resistivity ρ(T) measured at zero field in the temperature range of 80-300K, is shown in Fig. 6. It is readily observed that the resistivity dramatically increases with x(Ti) increasing, due to the replacement of some Mn^{3+}-O-Mn^{4+} bonds by Mn^{3+}-O-Ti^{4+} bonds. Indeed, the Ti^{4+} addition brings about a disorder at the B-site and breaks the electrical transport channels, it reduces the number of empty orbitals of Mn^{4+} and therefore, the double-exchange interaction channels are broken. Taking the sign of the temperature derivative of the resistivity (dρ/dT) as a criterion, we find that compounds with x=0, x=0.02 and x=0.05 exhibit a metallic to semiconductor transition, while for samples with x = 0.07 and x=0.1 doping, the high-temperature semiconducting state is maintained throughout the whole temperature range. The next paragraphs will detail on these two different behaviours. It should be stressed that the temperature $T_{M\text{-}SC}$, corresponding to the metal-semiconductor transition, shifts to lower values with increasing x, similarly to T_C (Table III), and it is not further noticed in our temperature range, for substituting ratios above 7 at.%. of Ti^{4+}. As mentioned earlier, the larger ionic radius of Ti^{4+} increases the average (Mn,Ti)-O distance, resulting in a decrease of the charge carriers bandwidth W (Table I) and thus in an increase of the resistivity [19,20].

4-2-1- Semiconducting behaviour

The variation of the electrical resistivity with temperature above $T_{M\text{-}SC}$ may be explained on the basis of two different models. The variable range hopping (VRH) model has been used to explain the electrical conduction at high temperature, that is, in the range $T_p < T < \theta_{D/2}$, (θ_D, Debye temperature), while the small polaron hopping (SPH) model is considered for temperatures above $\theta_{D/2}$ [21].

For the semi-conductive transport character, the conduction may operate in terms of:

1- The Mott variable range hopping (VRH) mechanism [22], which is expressed as:

$$\rho(T) = \rho_0 \exp(T_0 / T)^{1/4} \qquad \textbf{(3)}$$

where ρ_0 depends on the assumption made about the electron-phonon interaction and is considered as constant in most of the cases, although it is slightly affected by temperature [23]. T_0 is the characteristic VRH temperature, $T_0 = 16.\alpha^3/k_\beta.N(E_F)$ where $N(E_F)$ is the density of states at the Fermi level. Here, the T_0 value is evaluated from the slope of the plot ln(σ) vs. $T^{-1/4}$ (Fig. 7**)**. The constant α was taken as $2.22nm^{-1}$ [24].

2- The Emin-Holstein theory of adiabatic small polaron hopping model (ASPH) [24], which is expressed as:

$$\rho(T) = BT\exp(E_a / k_B T) \qquad \textbf{(4)}$$

where E_a is the activation energy for hopping conduction and B is the residual resistivity. Figure 8 shows the results for the ASPH model, in which the straight line is a fit to Eq. (4). The computed values of T_0, $N(E_F)$ and E_a for these two models are summarized in Table IV. Both models describe quite well our results in the semiconducting phase, although the second model (ASPH) gives the best square linear correlation coefficients (R^2). We may conclude then, that the transport properties are dominated by the small polaron hopping mechanism.

4-2-2- Low-temperature metallic behaviour

The electrical conduction in the ferromagnetic phase, below the metal-semiconductor transition at $T=T_{M\text{-}SC}$ is generally understood according to the double-exchange theory. In this model, the Mn^{3+}-O-Mn^{4+} coupling are responsible of the conduction mechanisms from the half-filled to the empty e_g orbital.

The following equations are generally used to fit the electrical resistivity data in the case of the manganites:

$$\rho = \rho_0 + \rho_1 T \qquad \textbf{(5)}$$

$$\rho = \rho_0 + \rho_2 T^2 \qquad \textbf{(6)}$$

$$\rho = \rho_0 + \rho_{2.5} T^{2.5} \qquad \textbf{(7)}$$

$$\rho = \rho_0 + \rho_2 T^2 + \rho_{4.5} T^{4.5} \qquad \textbf{(8)}$$

where ρ_0 is the resistivity due to grain/domain boundaries and point defects scattering [25], the term $\rho_1 T$ is a thermal diffusive conductive process, $\rho_2 T^2$ in Eqs. (6) and (8) represents the electrical resistivity due to the electron-electron scattering [26]. The term $\rho_{2.5} T^{2.5}$ is the electrical resistivity due to electron-magnon scattering process in the ferromagnetic phase [27]. The term $\rho_{4.5} T^{4.5}$ is a combination of electron-electron, electron-magnon and electron-phonon scattering processes [28, 29].

The experimental data at $T < T_{M\text{-}SC}$ for polycrystalline $La_{0.67}Ba_{0.33}Mn_{1-x}Ti_xO_3$ samples (x=0, 0.02 and 0.05) were fitted to the above four equations and the quality of these fitting was evaluated by comparing the squared linear correlation coefficients (R^2) obtained for each equation. Best results are obtained using Eq. (8). Plots of the electrical resistivity versus temperature and the best fits to the data are shown in Fig. 9. These fits show that the parameters ρ_0, ρ_2 and $\rho_{4.5}$ increase with the increase Ti-doping, according to the reduction of the double-exchange mechanism (DE) (Table V). Therefore, the metallic regime can be attributed to the electron-(phonon, magnon) scattering processes, which further demonstrates that the metallic regime occurs in the ferromagnetic phase.

5- Conclusions

In summary, we have reported the effect of the substitution of Mn by Ti on the structural, magnetic and electrical transport properties of $La_{0.67}Ba_{0.33}Mn_{1-x}Ti_xO_3$ system as a function of doping (x). The XRD analysis, along with the magnetic and resistivity measurements support the fact that Ti^{4+} ions substitute for Mn^{4+}. The results were then compared with those obtained by substituting Mn^{3+} by Cr^{3+}. These results show that the substitution by non magnetic tetravalent Ti significantly weakens the double exchange interactions and, as a result, T_C decreases stronger than in the case of the substitution by the magnetic trivalent element Cr^{3+}. The resistivity measurements show that, by increasing the metal doping, the resistivity increases and the metallic behaviour of $La_{0.67}Ba_{0.33}MnO_3$, observed below room temperature,

is destroyed. Electrical investigations show that the metallic behaviour of the resistivity below the metal-semiconductor transition is well fitted by the relation $\rho = \rho_0 + \rho_2 T^2 + \rho_{4.5} T^{4.5}$. On the other hand, the high temperature resistivity above $T_{M\text{-}SC}$ was explained using variable range hopping (VRH) and small polaron hopping (SPH) models.

Acknowledgments.

Authors acknowledge the Tunisian National Ministry of Higher Education, Scientific Research for a Grant and the Tunisia-France exchange program DGRS-CNRS project n° 09//R 11-52. Ma. Oumezzine joint Ph. D program Monastir-Rennes.

References

[1] R. Von Helmot, J. Wecker, B. Holzapfel, L. Schultz, K. Samwer, Phys. Rev. Lett. 71, 2331 (1993).

[2] S. Jin, T. H. Tiefel, M. McCormack, P. A. Fastnachr, R. Ramesh, and L. H. Chen, Science 264, 413 (1994).

[3] G. C. Xiong, Q. Li, H. L. Ju, S. N. Mao, L. Senapati, X. X. Xi, R. L. Greene, T. Venkatesan, Appl. Phys. Lett. 66, 1427 (1995).

[4] M. Ziese, Rep. Prog. Phys. 65, 143, (2002).

[5] A. J. Millis, P. B. Littlewood, B. I.Shraiman, Phys. Rev. Lett. 74, 5144 (1995).

[6] A. Moreo, S. Yunoki, E. Dagotto, Science 283, 2034 (1999).

[7] A. M. Bratkovsky, Phys. Rev. Lett. 82, 141 (1999).

[8] C. Zener, Physical Review 82 403 (1951).

[9] C. Martin, A. Maignan, B. Raveau, J. Mater. Chem. 6, 1245 (1996).

[10] K. H. Ahn, X. W. Wu, K. Liu, C. L. Chien, J. Appl. Phys. 81, 5505 (1997).

[11] J. Blasco, J. Garcia, J.M de Teresa, M. R. Ibarra, J. Perez, P. A. Algarabel, C. Marquina, C. Ritter, Phys. Rev. B 55, 8905 (1997).

[12] C. Osthover, P. Grunberg, R. R. Arons, J. Magn. Magn. Mater. 177-181, 854 (1998).

[13] A. Maignan, C. Martin, B. Raveau, Z. Phys. B : Condens. Matter 102, 19 (1997).

[14] J. Yang, Y. Q. Ma, R. L. Zhang, B. C. Zhao, R. Ang, W. H. Song, Y. P. Sun, Solid State Commun. 136, 268 (2005).

[15] Ma. Oumezzine, O. Peña, S. Kallel, T. Guizouarn, M. Oumezzine, J. Alloys Compd. 533 , 33 (2012).

[16] J. M. D. Coey, M. Viret, S. von Molnar, Adv. in Phys. 48 167 (1999).

[17] J. Rodriguez-Carvajal, Physica B: Condensed Matter 192, 55 (1993).

[18] N. Kallel, G. Dezanneau, J. Dhahri, M. Oumezzine, H. Vincent, J. Mag. Mag. Mater. 56-65, 261 (2003).

[19] P.G. Radaelli, G. Iannone, M. Marezio, H.Y. Hwang, S.W. Cheong, J.D. Jorgensen, D.N. Argyriou, Phys. Rev. B, 56, 8265 (1997).

[20] S.M. Kim, B.J. Yang, Q. Cai, D.X. Zhou, J.W. James, B.W. Yelon, E.P. Parris, D. Buddhikot, K.S. Malik, Physical Review B 71, 014433 (2005).

[21] N.F. Mott, Journal of Non-Crystal Solids 1, 1 (1968).

[22] N. Mott, Conduction in Non-Crystalline Materials, Clarendon, Oxford, 1993, pp. 17–23.

[23] R. Laiho, K.G. Lisunov, E. Lahderanta,¨ V.N. Stamov, V.S. Zakhvalinskii., Journal of Physics: Condensed Matter 13, 1233 (2001).

[24] D. Emin, T. Holstein, Physical Review B 13, 647 (1976).

[25] A. Urushibara, Y. Moritomo, T. Arima, A. Asamitsu, G. Kido, Y. Tokura, Physical Review B 51, 14103 (1995).

[26] P. Schiffer, A.P. Ramirez, W. Bao, S.-W. Cheong, Physical Review Letters 75, 3336 (1995).

[27] V. Sen, N. Panwar, G.L. Bhalla, S.K. Agarwall, Journal of Physics and Chemistry of Solids 68, 1685 (2007).

[28] G.J. Snyder, R. Hiskers, S. DiCarolis, M.R. Beasley, T.H. Geballe., Physical Review B 53, 14434 (1996).

[29] G. Venkataiah, P. Venugopal Reddy., Solid State Communications 136, 114 (2005).

Tables captions.

Table I: Refined structural parameters of $La_{0,67}Ba_{0,33}Mn_{1-x}Ti_xO_3$ at room temperature. Space group $\mathbf{Pm\bar{3}m}$. The numbers in parentheses are the estimated standard deviations to the last significant digit.

Table II: Refined structural parameters of $La_{0,67}Ba_{0,33}Mn_{1-x}Cr_xO_3$ at room temperature ($x \leq 0.1$). Space group $\mathbf{R\,\bar{3}\,C}$ (from ref.15).

Table III: Values of the magnetic transition temperature T_C and the Metal-Semiconducting transition temperature $T_{M\text{-}SC}$ for $La_{0,67}Ba_{0,33}Mn_{1-x}Me_xO_3$ (Me=Ti,Cr).

Table IV: Characteristic temperature T_0, density of states at the Fermi level $N(E_F)$, activation energy E_a and correlation factors R^2 for $La_{0,67}Ba_{0,33}Mn_{1-x}Ti_xO_3$ ($0 \leq x \leq 0.1$) using VRH (eq.3) and ASPH (eq. 4) models.

Table V: Fit parameters to equation (8) $\rho(T) = \rho_0 + \rho_2 T^2 + \rho_{4.5} T^{4.5}$, obtained for the metallic behaviour (below $T_{M\text{-}SC}$) for $La_{0,67}Ba_{0,33}Mn_{1-x}Ti_xO_3$ samples.

Figures captions:

Figure 1: X-ray diffraction patterns of $La_{0,67}Ba_{0,33}Mn_{1-x}Ti_xO_3$ ($0 \le x \le 0.1$) compounds at room temperature, indexed on a $Pm\bar{3}m$ space group.

Figure 2 : Rietveld refinement of X-ray diffraction data for $La_{0,67}Ba_{0,33}Mn_{1-x}Ti_xO_3$ ($0 \le x \le 0.1$). Open circles correspond to the X-ray diffraction data and the lines are theoretical fits to the observed X-ray data. Vertical bars are the Bragg reflections for the space group $Pm\bar{3}m$. The difference pattern between the observed data and the theoretical fit is shown at the bottom.

Figure 3: Variations of the lattice constant and cell volume (in inset) for $La_{0,67}Ba_{0,33}Mn_{1-x}Ti_xO_3$ ($0 \le x \le 0.1$).

Figure 4: SEM micrographs of $La_{0,67}Ba_{0,33}Mn_{1-x}Ti_xO_3$ samples (x = 0.05, 0.07 and 0.1).

Figure 5: (a) Plots of the magnetization, measured in a field of 0.01T, versus temperature for Ti-substituted $La_{0,67}Ba_{0,33}Mn_{1-x}Ti_xO_3$ in field-cooled (filled symbols) and zero-field-cooled (open symbols) modes. Inset shows the temperature derivative dM/dT, (b) T_C versus (Ti, Cr) content x.

Figure 6: Electrical transport data for $La_{0,67}Ba_{0,33}Mn_{1-x}Ti_xO_3$ ($0 \le x \le 0.1$).

Figure 7: Temperature dependence of the conductivity σ in scales of ln(σ) as a function of ($1/T^{1/4}$), for $La_{0,67}Ba_{0,33}Mn_{1-x}Ti_xO_3$ ($0.02 \le x \le 0.1$). The Variable Range Hopping (VRH) fits are also shown**.**

Figure 8: ln(ρ/T) versus 1/T plots in the high temperature region of $La_{0,67}Ba_{0,33}Mn_{1-x}Ti_xO_3$ samples ($0.02 \le x \le 0.1$). Full line is the fit to equation 4, $\rho(T) = BT\exp(E_a / k_B T)$.

Figure 9: Plots of the electrical resistivity ρ(T) for $La_{0,67}Ba_{0,33}Mn_{1-x}Ti_xO_3$ samples x = 0.02, and 0.05) and their fits (full lines) using equation 8, ($\rho(T) = \rho_0 + \rho_2 T^2 + \rho_{4.5} T^{4.5}$.

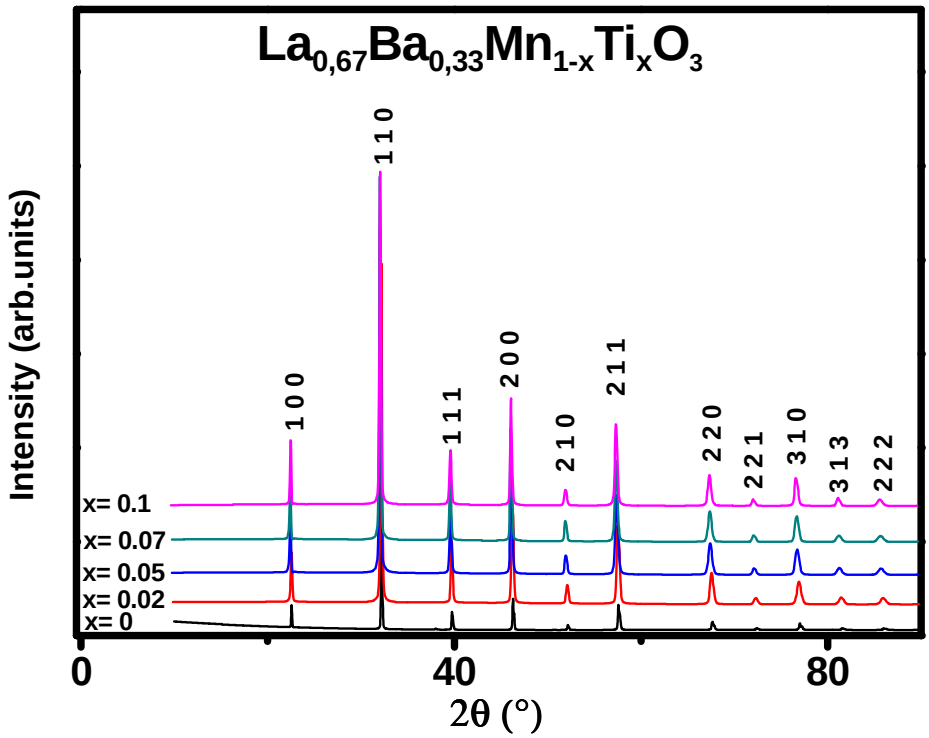

Figure 1 : X-ray diffraction patterns of $La_{0,67}Ba_{0,33}Mn_{1-x}Ti_xO_3$ ($0 \leq x \leq 0.1$) compounds at room temperature, indexed on a $Pm\bar{3}m$ space group.

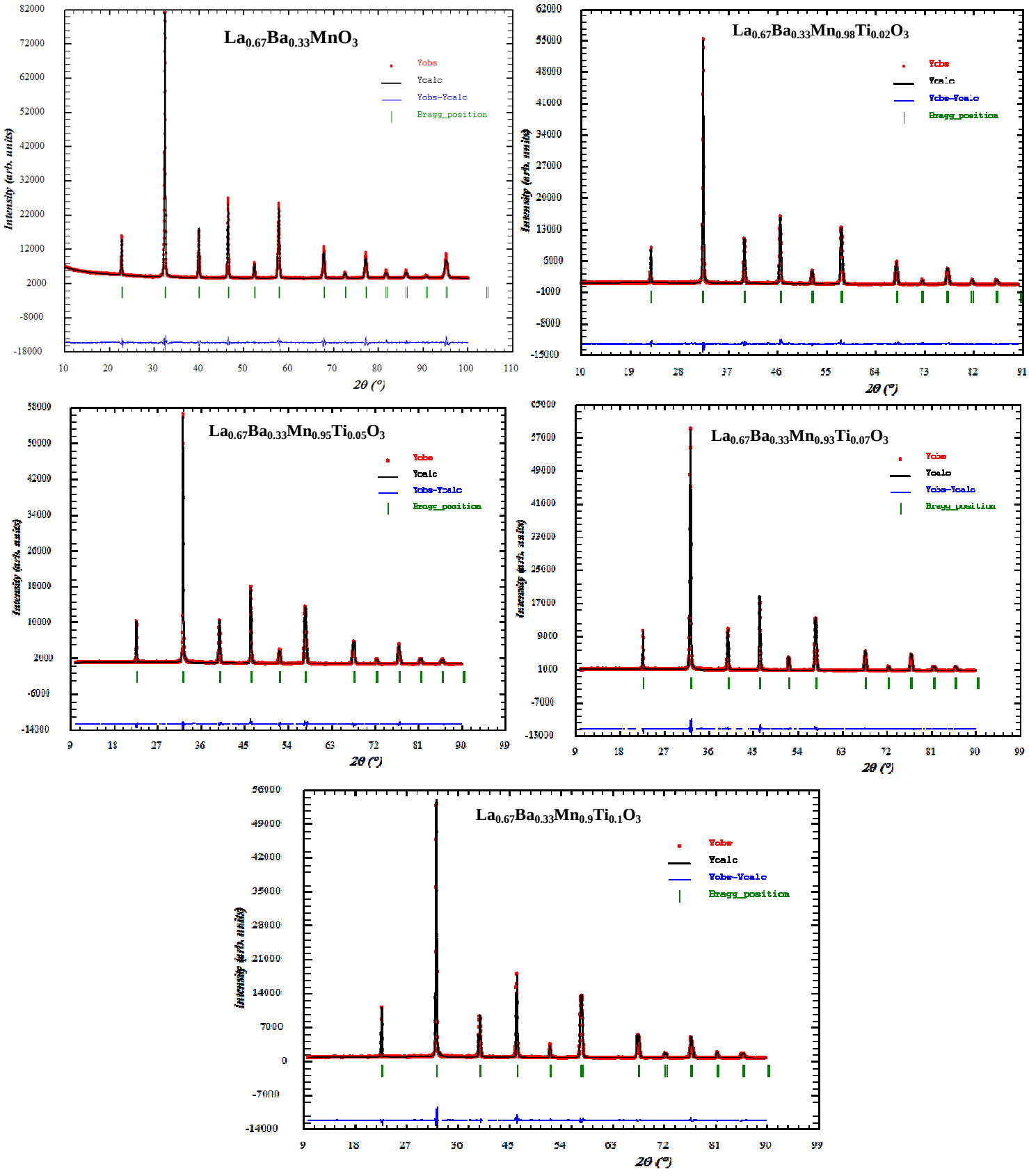

Figure 2 : Rietveld refinement of X-ray diffraction data for $La_{0,67}Ba_{0,33}Mn_{1-x}Ti_xO_3$ ($0 \le x \le 0.1$). Open circles correspond to the X-ray diffraction data and the lines are theoretical fits to the observed X-ray data. Vertical bars are the Bragg reflections for the space group $Pm\bar{3}m$. The difference pattern between the observed data and the theoretical fit is shown at the bottom.

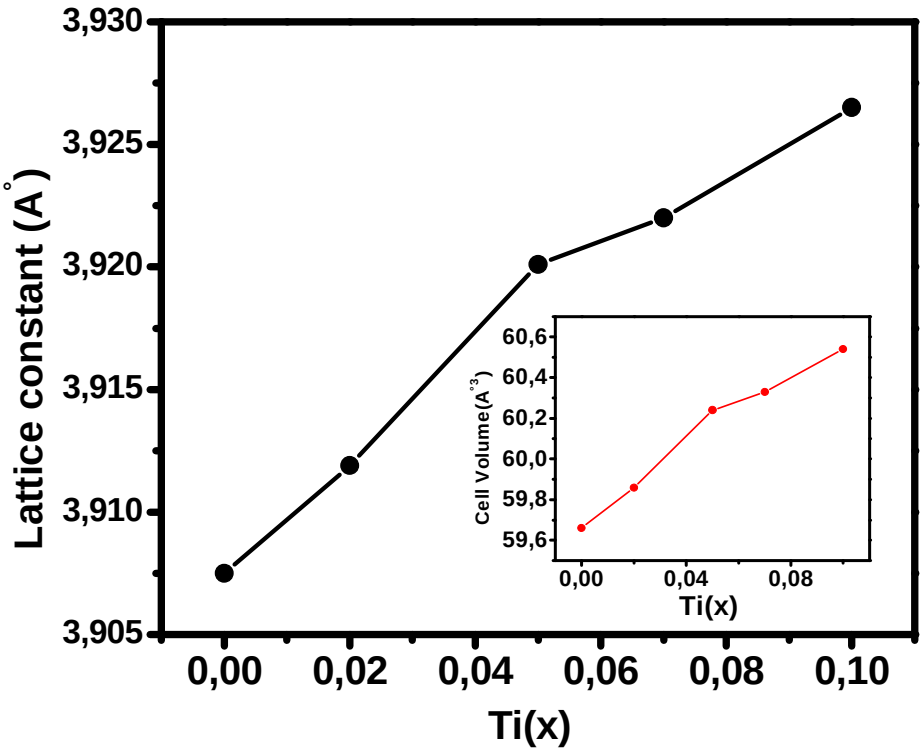

Figure 3: Variations of the lattice constant and cell volume (in inset) for $La_{0,67}Ba_{0,33}Mn_{1-x}Ti_xO_3$ ($0 \leq x \leq 0.1$).

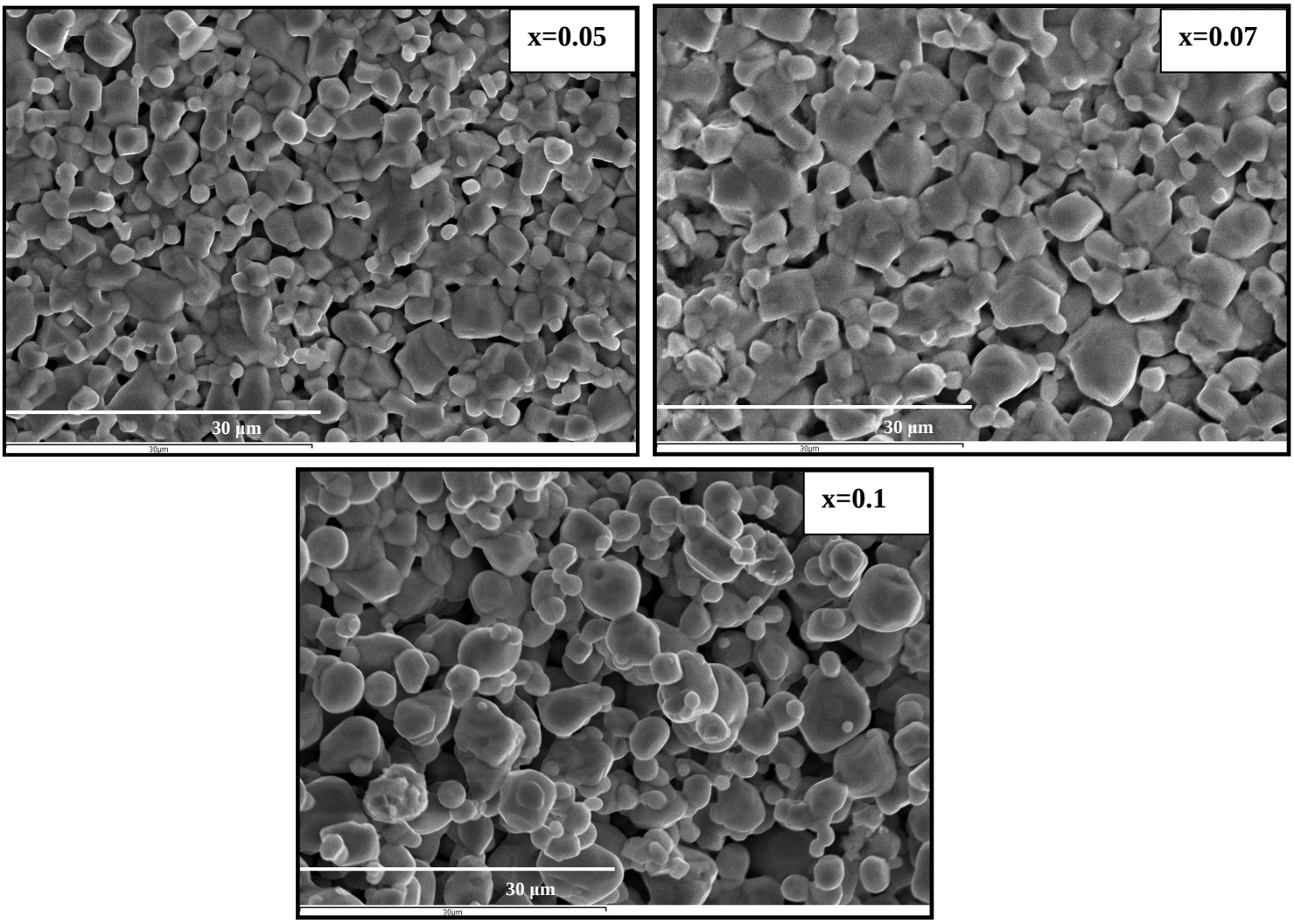

Figure 4: SEM micrographs of $La_{0,67}Ba_{0,33}Mn_{1-x}Ti_xO_3$ samples (x = 0.05, 0.07 and 0.1).

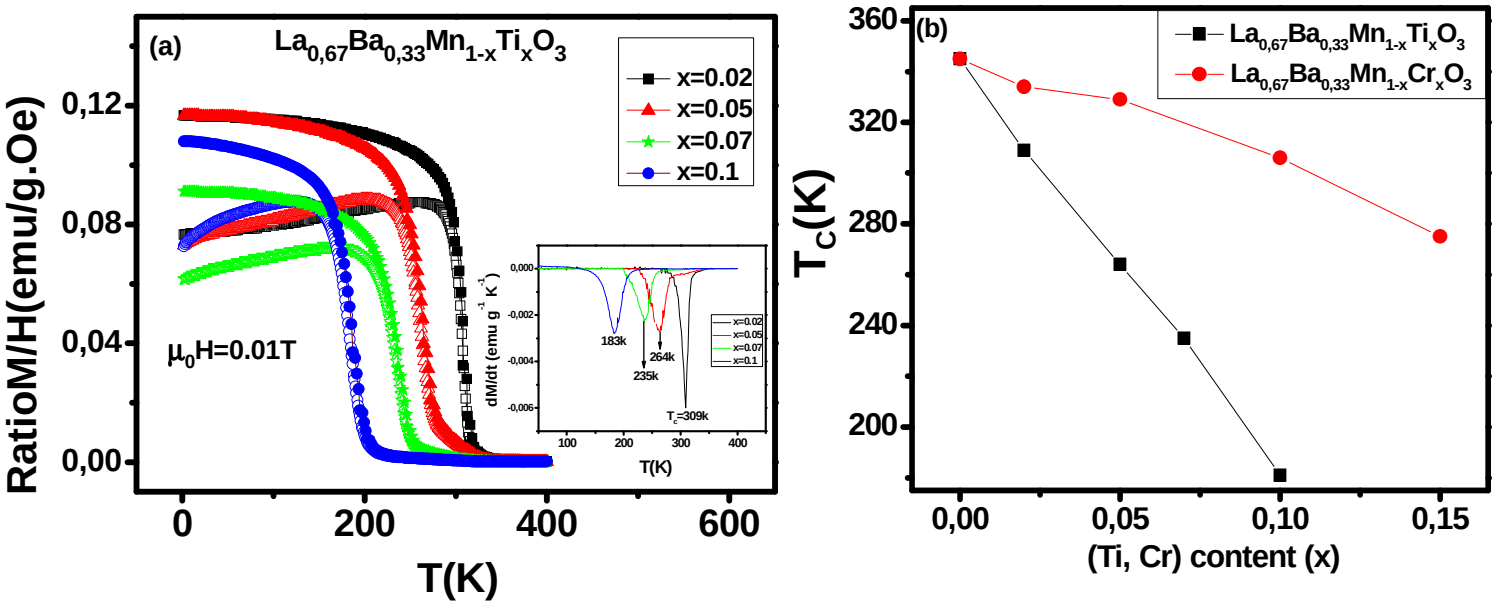

Figure 5: (a) Plots of the magnetization, measured in a field of 0.01T, versus temperature for Ti-substituted $La_{0,67}Ba_{0,33}Mn_{1-x}Ti_xO_3$ in field-cooled (filled symbols) and zero-field-cooled (open symbols) modes. Inset shows the temperature derivative dM/dT, (b) T_C versus (Ti, Cr) content x.

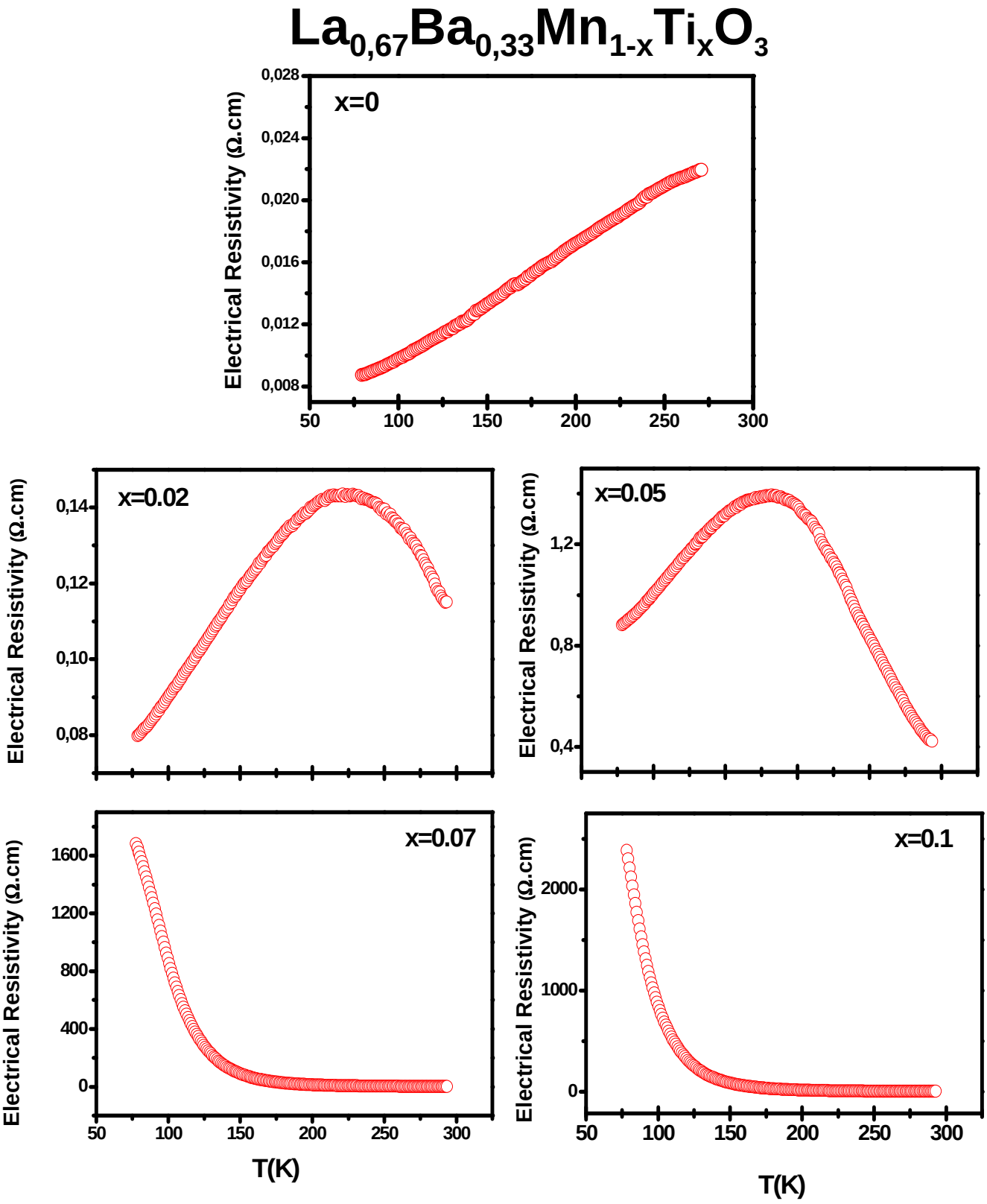

Figure 6: Electrical transport data for $La_{0,67}Ba_{0,33}Mn_{1-x}Ti_xO_3$ ($0 \le x \le 0.1$).

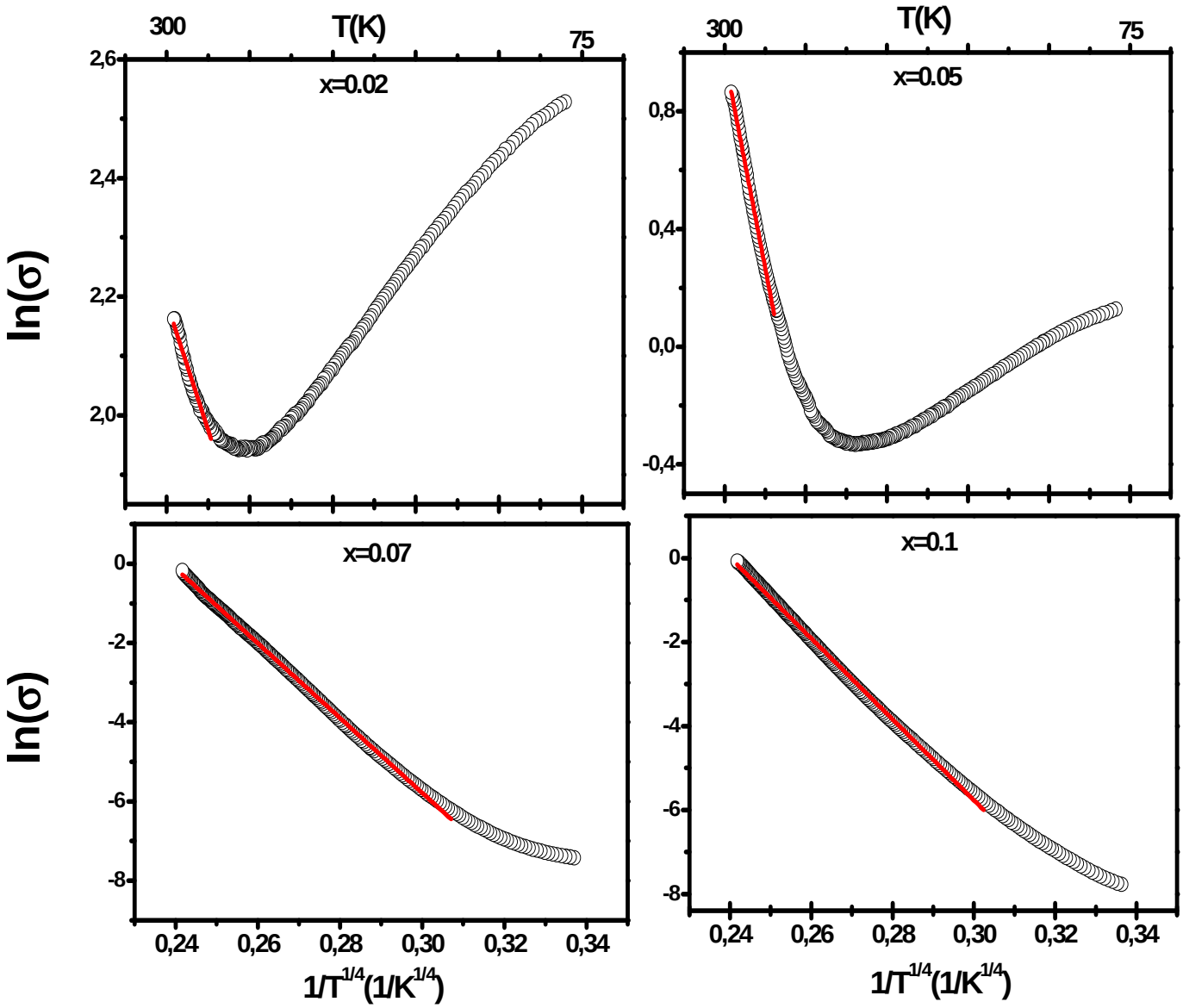

Figure 7 : Temperature dependence of the conductivity σ in scales of ln(σ) as a function of ($1/T^{1/4}$), for $La_{0,67}Ba_{0,33}Mn_{1-x}Ti_xO_3$ ($0.02 \le x \le 0.1$). The Variable Range Hopping (VRH) fits are also shown**.**

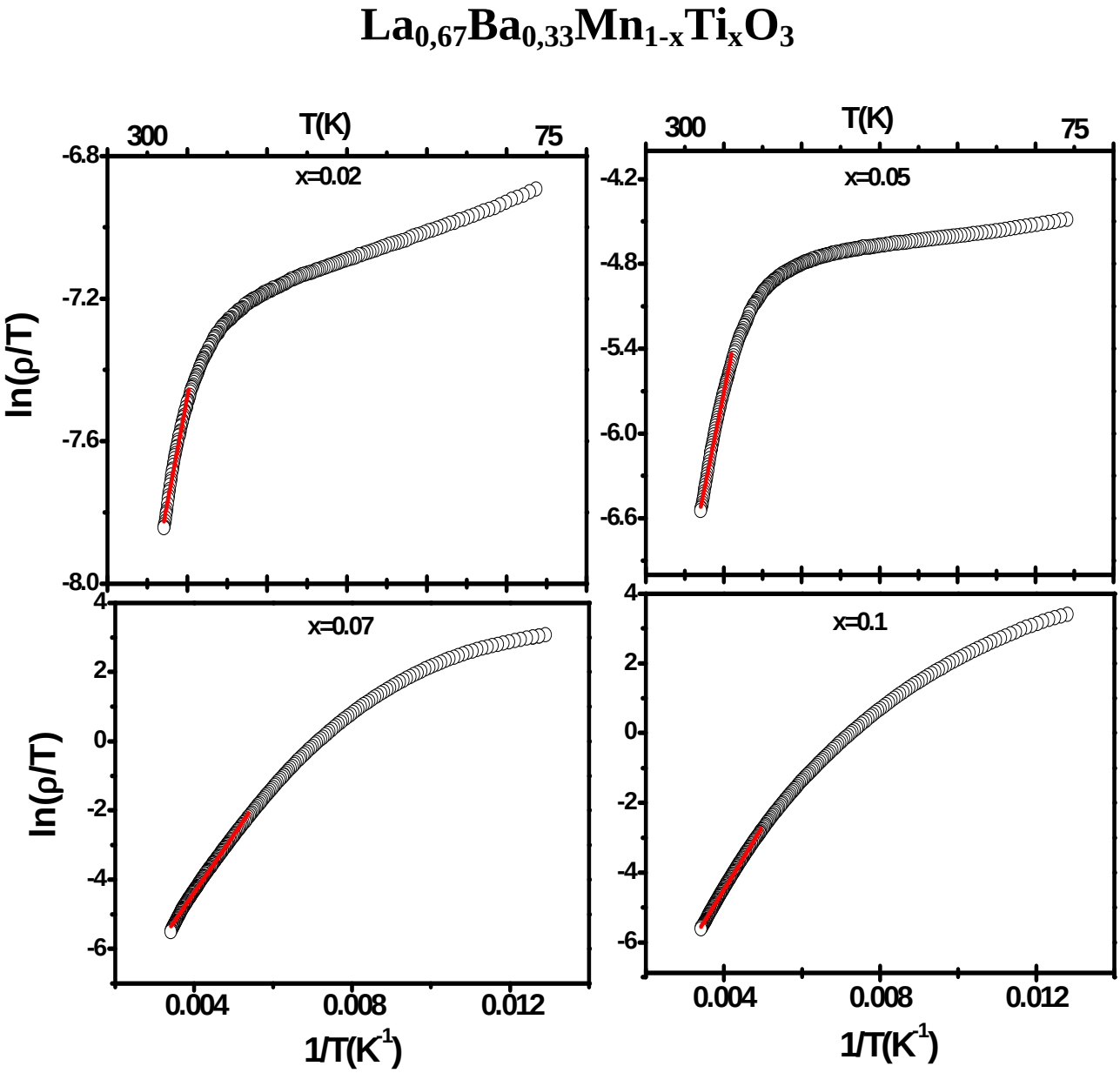

Figure 8 : ln(ρ/T) versus 1/T plots in the high temperature region of $La_{0,67}Ba_{0,33}Mn_{1-x}Ti_xO_3$ samples ($0.02 \le x \le 0.1$). Full line is the fit to equation 4, $\rho(T) = BT\exp(E_a / k_B T)$.

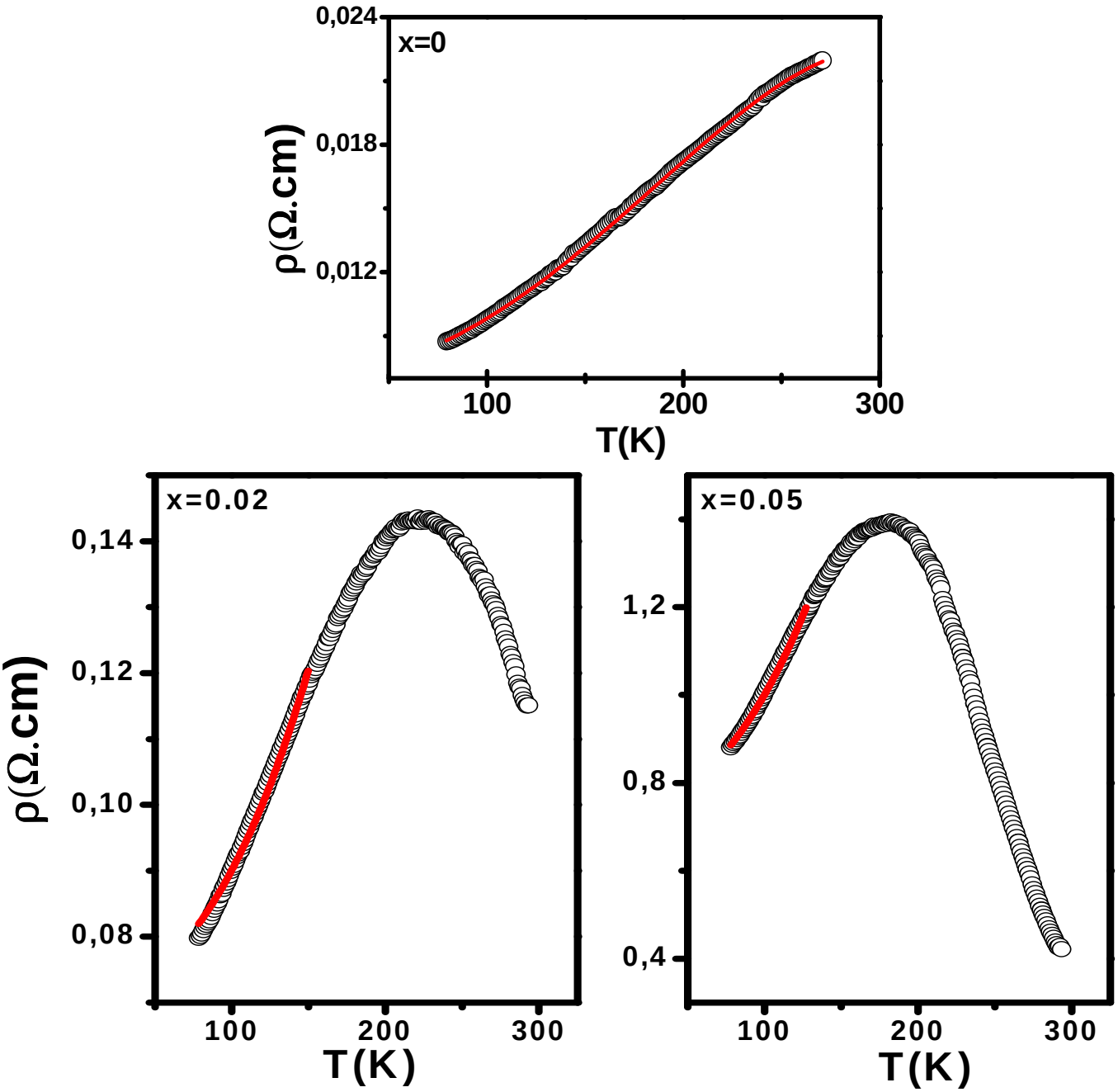

Figure 9 : Plots of the electrical resistivity ρ(T) for $La_{0,67}Ba_{0,33}Mn_{1-x}Ti_xO_3$ samples (x = 0, 0.02, and 0.05) and their fits (full lines) using equation 8, $\rho(T) = \rho_0 + \rho_2 T^2 + \rho_{4.5} T^{4.5}$.

Table I

Refined structural parameters of $La_{0,67}Ba_{0,33}Mn_{1-x}Ti_xO_3$ at room temperature. Space group **$Pm\bar{3}m$**. The numbers in parentheses are the estimated standard deviations to the last significant digit.

x	**0**	**0.02**	**0.05**	**0.07**	**0.1**
a(Å)	3.9075 (2)	3.9119 (2)	3.9201 (1)	3.922 (1)	3.9265 (1)
V ($Å^3$)	59.66 (0)	59.86 (1)	60.24 (0)	60.33 (0)	60.54 (0)
t_G	0.9999	0.9992	0.9981	0.9973	0.9962
La/Ba B_{iso} ($Å^2$)	0.32 (9)	0.08 (4)	0.85 (4)	1.18 (4)	1.01 (5)
Mn/Ti B_{iso} ($Å^2$)	0.02	0.066	0.44 (6)	0.75 (5)	0.26 (7)
(O) B_{iso} ($Å^2$)	2.03 (9)	1.20 (1)	1.6 (1)	2.44 (1)	2.1 (1)
$d_{(Mn, Ti)-O}$ (Å)	1.953 (5)	1.956 (2)	1.960 (5)	1.961 (4)	1.963 (5)
$\theta_{(Mn, Ti -O- Mn, Ti)}$ (°)	180 (8)	180 (2)	180 (6)	180 (5)	180 (6)
W (a.u)	0.0961	0.0955	0.0948	0.0946	0.0943
R-factor (%)					
R_{wp} (%)	3.38	5.03	4.27	4.15	5.24
R_p (%)	2.18	3.73	3.2	3.09	3.92
R_F (%)	1.94	3.16	2.36	1.69	1.97
χ^2 (%)	5.3	3.63	2.68	2.45	3.56

Table II

Refined structural parameters of $La_{0,67}Ba_{0,33}Mn_{1-x}Cr_xO_3$ at room temperature ($x \leq 0.1$).
Space group $\mathbf{R\bar{3}C}$ (from ref.15)

x	**0**	**0.02**	**0.05**	**0.1**
a (Å)	5.5322 (1)	5.5316(1)	5.5314 (1)	5.5315 (1)
c (Å)	13.5034 (2)	13.5004 (2)	13.4994 (1)	13.4922 (3)
V(Å$^{\circ}$)^3	357.91 (1)	357.75 (1)	357.70 (1)	357.52 (1)
$d_{(Mn, Cr)-O}$ (Å)	1.9550	1.9562(6)	1.9575 (4)	1.9587(9)
$\theta_{(Mn, Cr -O- Mn, Cr)}$ (°)	175.77 (2)	173.84(2)	172.42(5)	171.2(4)
W	0.0956	0.0954	0.0952	0.0948

Table III

Values of the magnetic transition temperature T_C and the Metal-Semiconducting transition temperature T_{M-SC} for $La_{0,67}Ba_{0,33}Mn_{1-x}Me_xO_3$ (Me=Ti,Cr)

Composition $La_{0,67}Ba_{0,33}Mn_{1-x}Me_xO_3$	**T_{M-SC} (K) Me=Ti**	**T_c (K)**	
		Me=Ti	**Me=Cr**
x=0	T_{M-SC}>300	345	345
x=0.02	224	309	334
x=0.05	181	264	329
x=0.07	____	235	____
x=0.1	___	183	306

Table IV

Characteristic temperature T_0, density of state at the Fermi level $N(E_F)$, activation energy E_a and correlation factors R^2 for $La_{0,67}Ba_{0,33}Mn_{1-x}Ti_xO_3$ ($0 \leq x \leq 0.1$) using VRH (eq. 3) and ASPH (eq. 4) models.

Composition $La_{0,67}Ba_{0,33}Mn_{1-x}Ti_xO_3$	**x=0.02**	**x=0.05**	**x=0.07**	**x=0.1**
VRH model				
T_0 (K)	7.33×10^5 (2)	3.51×10^7 (4)	8.45×10^7 (1)	10.02×10^7 (2)
$N(E_F)(ev^{-1}\ cm^{-3})$	2.77×10^{21}	5.78×10^{19}	2.40×10^{19}	2.03×10^{19}
$\mathbf{R^2}$	0.968	0.889	0.990	0.988
ASPH model				
E_a (meV)	64.80 (1)	118.02 (1)	143.09 (7)	157.53 (6)
$\mathbf{R^2}$	0.993	0.998	0.999	0.999

Table V

Fit parameters to equation (8) $\rho(T) = \rho_0 + \rho_2 T^2 + \rho_{4.5} T^{4.5}$, obtained for the metallic behaviour (below $T_{M\text{-}SC}$) for $La_{0,67}Ba_{0,33}Mn_{1-x}Ti_xO_3$ samples

Composition $La_{0,67}Ba_{0,33}Mn_{1-x}Ti_xO_3$	**x=0**	**x=0.02**	**x=0.05**
ρ_{max}(Ω-cm)	0.0219	0.1434	1.394
ρ_0(Ω-cm)	0.00709 (2)	0.0721 (1)	0.7223(2)
ρ_2(Ω-cm K^{-2})	2.703×10^{-7} (1)	1.821×10^{-6} (4)	2.52×10^{-5} (3)
$\rho_{4.5}$(Ω-cm $K^{-4,5}$)	5.24×10^{-15} (5)	1.91×10^{-11} (2)	2.69×10^{-10} (2)
R^2	0.998	0.997	0.996